Retinotopic mapping of adult human visual cortex with high-density diffuse optical tomography

Benjamin W. Zeff*, Brian R. White†, Hamid Dehghani‡, Bradley L. Schlaggar*, and Joseph P. Culver*§

*Department of Radiology, Washington University School of Medicine, St. Louis, MO 63110; †Department of Physics and School of Medicine, Washington University, St. Louis, MO 63130; and ‡Department of Physics, University of Exeter, Exeter EX4 4QJ, United Kingdom

Edited by Marcus E. Raichle, Washington University School of Medicine, St. Louis, MO, and approved May 29, 2007 (received for review December 19, 2006)

Functional neuroimaging is a vital element of neuroscience and cognitive research and, increasingly, is an important clinical tool. Diffuse optical imaging is an emerging, noninvasive technique with unique portability and hemodynamic contrast capabilities for mapping brain function in young subjects and subjects in enriched or clinical environments. We have developed a high-performance, high-density diffuse optical tomography (DOT) system that overcomes previous limitations and enables superior image quality. We show herein the utility of the DOT system by presenting functional hemodynamic maps of the adult human visual cortex. The functional brain images have a high contrast-to-noise ratio, allowing visualization of individual activations and highly repeatable mapping within and across subjects. With the improved spatial resolution and localization, we were able to image functional responses of 1.7 cm in extent and shifts of <1 cm. Cortical maps of angle and eccentricity in the visual field are consistent with retinotopic studies using functional MRI and positron-emission tomography. These results demonstrate that high-density DOT is a practical and powerful tool for mapping function in the human cortex.

functional brain mapping | near-infrared spectroscopy | neuroimaging | retinotopy

Functional mapping of the human brain is an important aspect of cognitive neuroscience that is used to study brain organization and development. Increasingly, functional neuroimaging is being used as a diagnostic and prognostic tool in the clinical setting. Its expanding application in the study of disease and development necessitates new, flexible functional neuroimaging tools. Many situations are not amenable to scanner logistics, such as subjects who are in the intensive care unit, who are performing complex tasks, or who might otherwise require sedation for imaging, such as infants and young children. Additionally, there are imaging situations in which the neurovascular coupling either is not mature, such as in neonates and very young infants (1–3), or is altered due to injury or illness (4, 5). Diffuse optical imaging (DOI) is a methodology uniquely suited to such tasks, because it is a mobile system that uses a small, flexible imaging cap (6, 7). DOI images hemodynamic contrasts similar to functional MRI (fMRI) with blood oxygen-level dependent (BOLD) signals (fMRI-BOLD); however, DOI can measure changes in oxygenated hemoglobin (ΔHbO_2), deoxygenated hemoglobin (ΔHb_R), and total hemoglobin (ΔHb_T), whereas the BOLD signal is mainly dependent on ΔHb_R (8). The ability to simultaneously image these contrasts allows DOI to distinguish differences in their magnitude (3, 4, 9), timing (3, 10–12), and localization (13–15), forming a more complete picture of neurovascular function. In contrast to positron emission tomography (PET), which uses ionizing radiation, DOI uses safe, infrared light for imaging. Despite unique strengths, however, DOI as a standard tool for functional mapping has been limited by low spatial resolution, a lack of volumetric localization, and instrument complexity. We have developed an optical imaging system with superior contrast-to-noise characteristics that overcomes many previous limitations to provide higher resolution imaging while maintaining simple instrumentation.

The vast majority of DOI studies have been performed in topographic mode, in which the image is synthesized from measurements at a single source–detector pair (SD pair) separation and without overlapping measurements. Topographic DOI has been used extensively, for example, to map functional responses in the human visual (16–18), sensorimotor (13), and auditory cortex (19, 20); to study language lateralization in the prefrontal cortex (21); to record brain activity in infants (3, 17, 19, 20, 22–24); and even to measure cerebral blood volume during seizures (25, 26). Topographic DOI has limited lateral resolution and no depth-sectioning capability, precluding spatial separation of superficial and brain signals. Because of these limitations, topography studies of the visual cortex have been limited to distinguishing contralateral activations, an imaging task requiring no greater than 4-cm resolution.

A more advanced optical imaging method, diffuse optical tomography (DOT), relies on a variety of measurement strategies to improve lateral resolution and acquire depth information. Time-resolved measurements, for example, use time-gating to profile different tissue depths (27–31). However, the complexity and cost of time-resolved systems impose practical limits and require tradeoffs between channel count, optode density, coverage (field of view), and frame rate. Another strategy is to use high-density DOT grids, which use overlapping measurements at multiple SD pair separations (32, 33); different measurement distances provide information about different depths, and the use of overlapping measurements improves lateral resolution and localization. However, due to the large range in measured light levels, this approach places very stringent requirements on dynamic range and channel cross-talk. Despite these challenges, initial reports on DOT of the human brain demonstrate the feasibility of detecting lateralization of motor cortex activation (24, 27, 34), cerebral hemorrhage, decreased brain oxygenation in neonates after acute stroke (35), and vascular responsivity during the Valsalva maneuver (36). The breadth of these applications highlights the promise of the tomographic approach to optical neuroimaging.

In this paper, we report functional mapping of the adult human visual cortex made possible by a high-density DOT imaging system. The visual cortex is ideal for testing new

Author contributions: B.W.Z., B.L.S., and J.P.C. designed research; B.W.Z., B.R.W., and J.P.C. performed research; B.W.Z. B.R.W., H.D., and J.P.C. contributed new reagents/analytic tools; B.W.Z., B.R.W., and J.P.C. analyzed data; and B.W.Z., B.R.W., B.L.S., H.D., and J.P.C. wrote the paper.

The authors declare no conflict of interest.

This article is a PNAS Direct Submission.

Abbreviations: ADC, analog-to-digital converter; DOI, diffuse optical imaging; DOT, diffuse optical tomography; fMRI, functional MRI; PET, positron-emission tomography; SD pair, source–detector pair.

§To whom correspondence should be addressed. E-mail: culverj@wustl.edu.

This article contains supporting information online at www.pnas.org/cgi/content/full/0611266104/DC1.

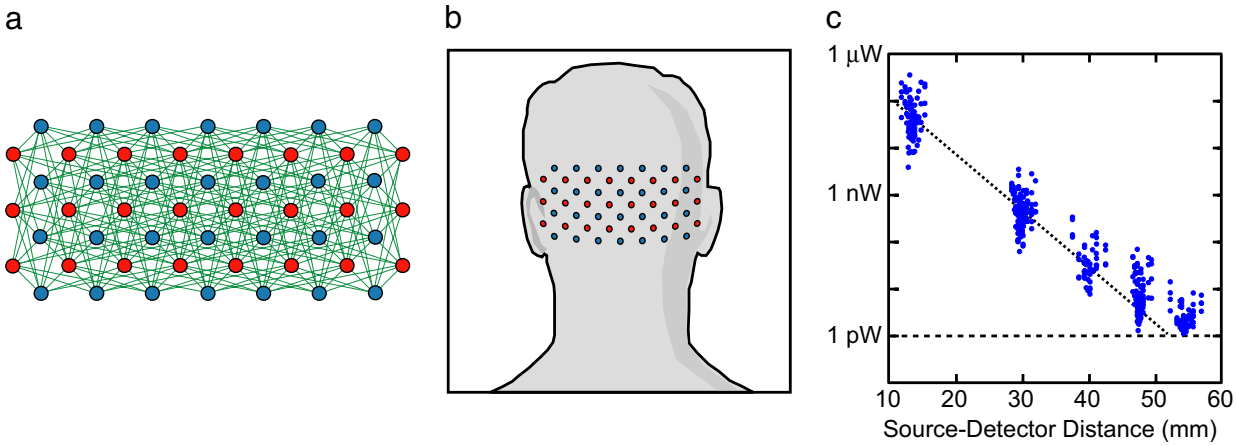

Fig. 1. High-denisty DOT system. (*a*) Schematic of the high-density imaging grid with 24 sources (red) and 28 detectors (blue). Measurement pairs are represented by green lines. We used first-, second-, third-, and fourth-nearest-neighbor pairs at source–detector separations of 13, 30, 40, and 48 mm, respectively. (*b*) Schematic showing the placement of the imaging grid over the visual cortex. (*c*) Detected light level vs. source–detector separation on a human subject averaged over 1 sec (≈10 image frames). All first-, second-, third-, and fourth-nearest-neighbor pairs were detected simultaneously and were well above the noise floor (dotted line).

neuroimaging techniques because its structure and function have been comprehensively mapped with invasive anatomical and electrical studies in mammals (37–39) and in humans (40–42). Visual cortex activations were used extensively in early evaluations of PET and fMRI as functional brain mapping tools (43–46). More recently, the visual cortex was used as a model system to establish fMRI procedures for comparative mappings of adults and children in a common stereotactic space (47). Whereas previous optical imaging studies of the visual cortex have focused on discriminating contralateral activations (15, 18), here we report functional features of the human visual cortex that were previously inaccessible to optical imaging, such as eccentricity within quadrants of the visual field. These retinotopic mappings are repeatable and are consistent with previous fMRI and PET mappings. A high contrast-to-noise ratio allows us to measure individual activations, enabling us to move beyond repetitive block design stimulus paradigms. We present imaging of an angular sweep of the visual field that highlights these capabilities. The imaging improvements of this high-density DOT system, as demonstrated in these retinotopic maps, constitute a large step toward the full realization of optical imaging for mapping brain function in humans.

Results

A basic tenet of our DOT instrument design is to move as much of the system control and signal processing into the digital domain as possible. Such an approach simplifies system integration, increases the flexibility of the system, increases the effective dynamic range, and reduces channel cross-talk between SD pair measurements. One common limitation of previous DOT systems has been the use of time-shared, multiplexed, 16-bit analog-to-digital converters (ADCs), which generally have poor channel cross-talk values of more than −80 dB (10^{-4}). With time-encoding of sources, dynamic gain adjustments can be made before the ADC to increase the effective dynamic range and cross-talk rejection (34, 48–50). However, dynamic gain adjustments at high speeds become increasingly complex and prone to new sources of channel cross-talk.

For the design of our continuous wave high-density DOT imager, we took a different approach, instead using isolated detector channels digitized with dedicated 24-bit ADCs. Dedicated control lines for each source are used for flexible software-configurable source encoding (frequency-, time-, and spatial-encoding). This design provides high instantaneous dynamic range ($>10^6$) and cross-talk rejection ($<10^{-6}$), so that light levels over many orders of magnitude can be detected simultaneously. The instrument has two near-infrared wavelengths (750 and 850 nm) at each of 24 source positions. The sources are interleaved with 28 detectors in a high-density array (Fig. 1*a*) with overall dimensions of 13.2 × 6.6 cm. The optical fibers were coupled to the head with a flexible, plastic cap molded to fit the back of the head over the visual cortex (Fig. 1*b*). Each detector samples light from all sources, for a total of 672 possible measurements.

With the high sensitivity and dynamic range of the instrument, first- (13 mm), second- (30 mm), third- (40 mm), and fourth-nearest-neighbor (48 mm) optode pairs (and greater in certain situations) can be sampled simultaneously, with light levels well above the noise floor, for a total of 348 measurements (Fig. 1*c*). For comparison, a recently demonstrated system using 16-bit ADC showed that mixed time- and frequency- encoding can extend the dynamic range (70–80 dB) sufficiently to record with second-nearest-neighbor pairs in a hexagonal optode pattern at a rate of 1.2 Hz (34). In contrast, our system has a 10 times faster frame rate (12 Hz) with a dynamic range of 120 dB. The increased dynamic range and cross-talk rejection of our 24-bit system permits the use of a more densely sampled rectangular array with measurements out to fourth-nearest-neighbor.

Eccentricity Mapping. As a result of the dense spatial sampling and the removal of global and superficial signals, functional activations had high contrast-to-noise ratios (CNR) (e.g., in Fig. 2, CNR = 12:1 without block averaging and CNR = 34:1 with block averaging), and activations due to even single stimuli could be imaged (Fig. 2). As evident in Fig. 2*b*, the activations are localized at depth with very little change in hemoglobin present in the outer layer. In Fig. 2*c*, a time series of cortical projection images are depicted for ΔHbO_2 concentration. Fig. 2*d* shows a time trace of ΔHbO_2, ΔHb_R, and ΔHb_T in a high-activation 1-cm^3 region for nine individual stimuli, demonstrating strong activation. The measured hemoglobin time courses are in good agreement with previous fMRI and DOI studies (51). In a movie of nine individual functional activations from one imaging session (without block averaging) the localized activation is clearly visible in response to each presentation of the stimulus [supporting information (SI) Movie 1]. A typical time course (Fig. 2 *c* and *d*) shows a peak in the functional signal at t = 11 sec (stimulus presentation, t = 0–10 sec).

To map eccentricity, three stimulus types were presented: a

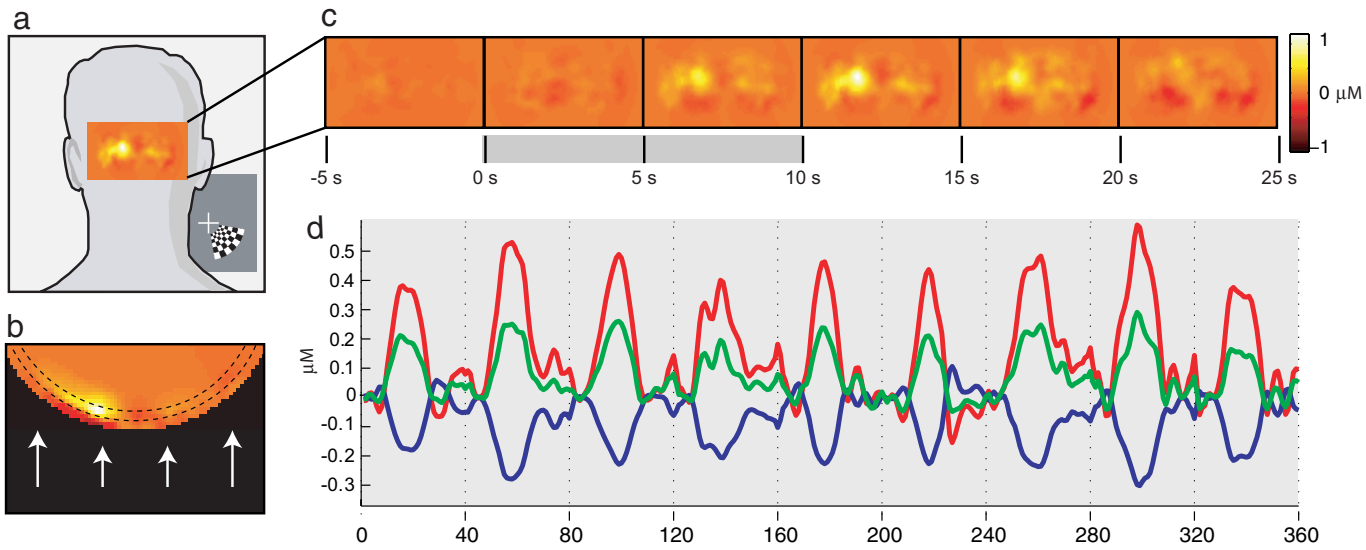

Fig. 2. Detection of visual cortex activations. (*a*) Schematic showing placement of activation images on a human subject. (*Inset*) The visual stimulus presented is a reversing, radial grid (10-Hz reversal) that is black and white on a 50% gray background and that extends over a polar angle of 70° and a radial angle of 0.5–1.7°. (*b*) An axial image slice with a cortical activation (subject 4). In this paper, images are displayed as two-dimensional coronal projections (as in *c*) of a cortical shell covering a depth 10 ± 2 mm below the scalp surface (the region between dotted lines with arrows showing direction of view). (*c*) Time course showing the temporal response of ΔHbO_2. The stimulus occurred during t = 0–10 sec. (The color scale applies to *a*–*c*.) (*d*) The high-density grid allows imaging of functional activations from individual stimuli, shown here for nine of the same stimulus (ΔHbO_2, red; ΔHb_R, blue; ΔHb_T, green) (subject 5).

central lower-right grid (stimulus A), a peripheral lower-right grid (stimulus B), and a central lower-left grid (stimulus C) (Fig. 3*a*). All three stimuli were radial, reversing, black-and-white grids (10-Hz reversal) on a 50% gray background presented sequentially in a block paradigm, with each block being a 10-sec stimulus presentation followed by a 30-sec 50% gray screen (Fig. 3*a*). Fig. 3 *b*–*f* show

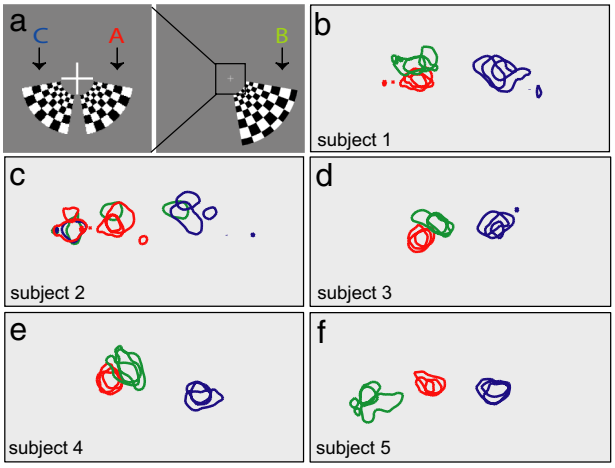

Fig. 3. Eccentricity mapping in the visual field was evaluated within and across five subjects. (*a*) Schematics of the visual stimulus. (*Right*) The full screen subtended a radial angle ± 12°. The peripheral lower-right stimulus (B) extended over a polar angle of 70° and a radial angle of 2.5–10.5°. (*Left*) An expanded view of the central view area showing the central lower-right stimulus (A) that extends over a polar angle of 70° and a radial angle of 0.5–1.7°. The central lower-left stimulus (C) mirrors stimulus A. (*b*–*f*) Contours at 75% maximum for peak (ΔHbO_2) activations A (red), B (green), and C (blue) for three sessions for each of five subjects show the repeatability of the measurements and highlight their spatial resolution. Each of the five subjects was imaged in three distinct sessions, with nine of each stimulus (A–B–C) presented in each session. The activations for each session and stimulus type were block-averaged. Contours were obtained from projection images (as in Fig. 2*c*) averaged over t = 7–15 sec.

functional maps for the eccentricity stimuli using 75% maximum contours (averaged over the peak ΔHbO_2 temporal response, t = 7–15 sec) for each subject (three stimuli in each of three sessions; the data from different scans within the same session were block-averaged together). The images for each subject were coregistered by applying a linear transformation to account for intersession variability in cap placement (see *Methods*). Threshold maps for each subject and contrast, averaged across all three sessions, are shown in SI Fig. 6 (coronal projection) and SI Fig. 7 (axial). In subjects 1, 3, 4, and 5, strong localized activations were seen in response to all three stimuli. In subject 2, the activation maps were less localized and had higher noise. The average centroids of the activations (ΔHbO_2) are (relative to the center of the imaging pad): central lower-right (stimulus A: $x = -20$ mm, $z = 0$ mm), peripheral lower-right (stimulus B: $x = -20$ mm, $z = 5$ mm), and central lower-left (stimulus C: $x = 17$ mm, $z = 1$ mm). Here, x denotes the horizontal axis and z represents the vertical axis. Intersubject variability is evident in the relative positions of mappings of the three stimuli. The centroids for the central lower-right and the central lower-left were separated by $\Delta x_{AC} = 37 \pm 4$ mm and $\Delta z_{AC} = 1 \pm 5$ mm (mean ± SD). The intersubject variability is more pronounced when examining the A–B shift. Relative to the centroid of activation A, the centroid of activation B is shifted by $\Delta x_{AB} = 0 \pm 13$ mm and $\Delta z_{AB} = 4 \pm 7$ mm. The variation is most easily understood if we express the A–B separation in polar coordinates with the origin being the centroid of activation A and $\theta = 0°$ corresponding to a positive horizontal (x) axis. Then the shift is a radial separation of $\Delta r_{AB} = 13 \pm 7$ mm over an angular range of 167° with $\Delta\theta_{AB} = 83 \pm 67°$. So the radial separation of the two centroids is relatively constant with the majority of the variation coming from the angular component. This is consistent with visual inspection of Figs. 3 and 6, where (with the exception of noisy subject 2) the activations from the peripheral stimulus (B) are variable but appear in an annulus surrounding the activation from the central stimulus (A).

The activations for all five subjects were combined with a weighted average (Fig. 4). The data from different subjects was weighted by the peak contrast of each so that data from subjects with stronger activations was weighted more heavily. Here, the

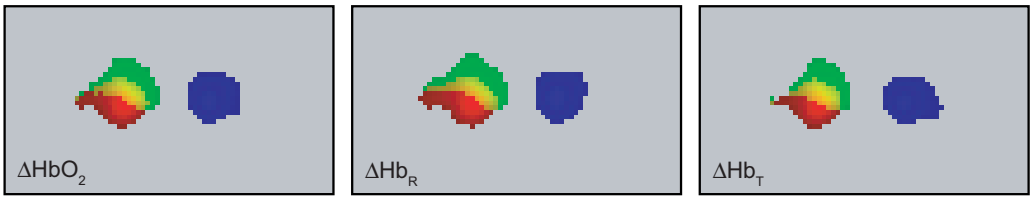

Fig. 4. Data above half-maximum value overlays of contrast-weighted average activations ($n = 5$ subjects) for all three stimuli (A, red; B, green; C, blue; with yellow being the overlap of the red and green channels) and contrasts (ΔHbO_2, ΔHb_R, and ΔHb_T). The central lower-right (A) and central lower-left (C) stimuli produce activations that are centered at (−21 mm, 0 mm) and (19 mm, 2 mm), respectively, relative to the center of the image. This separation is well matched with fMRI studies. The peripheral lower-right (B) stimulus results in an activation shifted medially and superiorly (center at −16 mm, 7 mm), consistent with angular and eccentricity maps of the human visual cortex from PET and fMRI studies.

activation regions above half maximum are shown for each of the three stimuli and for each contrast (ΔHbO_2, ΔHb_R, and ΔHb_T). Fig. 4 highlights the resolution of the system. Activations have spreads (FWHM ΔHb_T) of 18 mm for activation A, 17 mm for activation B, and 20 mm for activation C. The separations of the centroids are $\Delta x_{AC} = 41$ mm and $\Delta z_{AC} = 2$ mm and $\Delta x_{AB} = 4$ mm and $\Delta z_{AB} = 7$ mm (due to the weighting, the separation of the means is not the mean of the separations of individual subjects). In our polar representation, we have $\Delta r_{AB} = 8$ mm, $\Delta\theta_{AB} = 56°$ (above the x axis). Individual activation maps for subjects 1 and 3–5 show better distinction between stimuli than the group average maps (SI Fig. 6). For the group-averaged data (Fig. 4), the overlap (number of voxels above half-maximum contrast common to both activation maps and normalized to the average extent of the individual maps) of stimuli A and B is 42% (overlaps for ΔHbO_2, ΔHb_R, and ΔHb_T are similar within ±2%). For the individual maps (Fig. 6), overlap values range from 0% to 42%, with a mean of 24%.

Polar Angle Mapping. The second visual paradigm was an angularly swept radial reversing grid (10-Hz reversal, 10°/sec). Fig. 5*a* shows images from the sweep data for subject 5. The 30 full-sweep cycles (36 sec each) were averaged together and down-sampled to 1 Hz to create 36 images with 10° phase separation. Four time points separated by 90° phase were chosen to yield a set of four activations symmetric across the midline. The four stimuli shown, also separated by 90° phase shifts, represent a 4.5-sec shift relative to the functional activations with which they were matched. Half-maximum contours of the four activations are shown in Fig. 5*b*. In a movie of the entire sweep (30 cycles averaged together), the mapping of retinal polar angle is clearly visible (SI Movie 2).

Discussion

Our results provide eccentricity maps within a visual field quadrant and angular mapping of the visual cortex created with DOT. We find good agreement with fMRI and PET retinotopic maps. For example, it is known from anatomical and functional studies (52) that the particular pattern of cortical folding and, thus, the localization and borders of functional responses vary significantly between individuals. Therefore, differences in the measured positions of the visual cortex activations are expected. The mean central-left to central-right separations measured by our DOT system are $\Delta x_{AC} = 37 \pm 4$ mm and $\Delta z_{AC} = 2 \pm 5$ mm. These values are in good agreement with fMRI studies of the adult visual cortex ($\Delta x = 42$ mm and $\Delta z = 4$ mm, with SD values reported in the range 3–7 mm) (47). It is difficult to compare the relative mapping of the central and peripheral lower-right stimuli ($\Delta x_{AB} = 4$ mm and $\Delta z_{AB} = 7$ mm) to the common, unfolded space used in the visualization of fMRI data. However, the vertical shift of the activation is quantitatively in agreement with PET eccentricity maps (53) and qualitatively supported by angular and eccentricity maps performed with fMRI (54, 55). Heuristically, we can explain the DOT eccentricity maps as a shift from the perimacular retina, which maps with a large projection onto the lateral occipital cortex, to the peripheral retina, which is largely projected within the calcarine sulcus along the midline. In addition, one would expect a large anterior shift. Although such depth profiling may be possible in infants, the depth sensitivity of our current study does not readily reveal this shift.

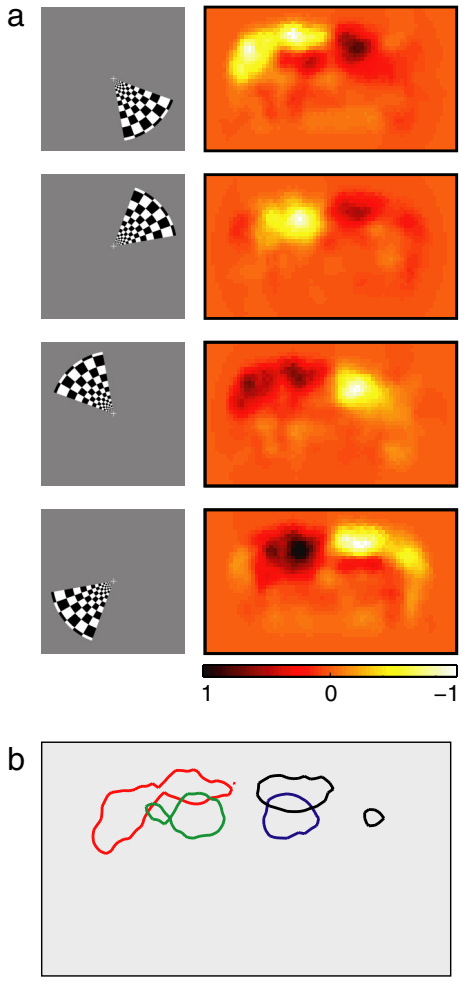

Fig. 5. Polar angle mapping with DOT. (*a*) Functional responses to an angularly swept grid (subject 5). The grid (60° polar angle, 0.5–10° radial angle, reversed at 10 Hz) was rotated in steps of 10° (polar angle) each second. The successive stimulus and activation images have a phase shift of 90° from the previous image. Color maps were normalized within each frame to plus or minus maximum contrast (0.34, 0.60, 0.45, and 0.32 μM, top to bottom respectively). (*b*) Half-maximum contours of the four activations show the left–right symmetry of the mapping for the angular sweep.

Interestingly, several of the maps show regions of apparent deactivation or negative contrast. For the polar mapping (Fig. 5), negative voxels are likely due to the temporal analysis that enforces a zero-mean value to the data. In the axial slices of Fig. 2*b*, negative voxels in the superficial layers are possibly the result of artifacts from the reconstruction process (e.g., ripples in the effective point spread function). In the time-course projection images of Fig. 2 *a* and *d*, the negative contrast may be due to either deactivation, residual image noise, or more subtle reconstruction artifacts. Future validation studies using coregistered MR structural and functional data are needed to resolve these issues (34, 56).

The high-density DOT system presented is able to reproduce activations within a subject over multiple imaging sessions. This reproducibility allowed us to detect significant intersubject variability, which has important consequences for more detailed cortical mapping problems (e.g., identifying borders of visual cortical areas). In addition, the robust intrasubject results show that DOT offers promise for single-subject mapping studies, where relying on an average map is insufficient, such as presurgical seizure focus localization or when optical contrasts are imaged intraoperatively on the cortical surface (57). High-density DOT arrays have the potential to map individual patients noninvasively. We look forward to application of the DOT imager to many of these interesting imaging problems.

For all of these applications, a necessary step in the development of DOT is the coregistration of DOT maps with anatomical images. In this study, in the interests of simplicity, DOT images were reconstructed in a hemispherical head model (see *Methods*), and, in the absence of anatomical data, we used the center of mass of the activation images for coregistration. A preferred approach would use a standard, MRI-derived head model for the forward light modeling to improve imaging accuracy and allow the DOT maps to be overlaid on an anatomical image (58, 59). Additionally, improving measurement of the placement of the DOT array relative to external landmarks on the head will allow the functional and anatomical images to be more accurately coregistered (24).

Conclusion

The inherent strengths of DOT are well established. Cap-based imaging is suitable for a wide range of imaging situations, and the ability to measure changes in HbO_2, Hb_R, and Hb_T can produce a more complete picture of brain function. However, the use of DOI has been hindered by insufficient spatial resolution and depth-sectioning and the greatly increased complexity of larger arrays. As our results demonstrate, high-density DOT is a significant step forward in resolving many of these obstacles to widespread use of DOT in neuroimaging by providing high contrast-to-noise functional signals, improved lateral resolution, and improved volumetric localization. We anticipate that these advancements in image quality will open the path to a wide range of new studies in the developing and diseased brain. Additionally, the modular design of the DOT system simplifies scalability to allow for mapping of larger cortical regions. These retinotopic maps in adult humans clearly indicate that high-density DOT can be a practical and powerful tool for functional brain mapping.

Methods

DOT Imaging System. Source light-emitting diodes (LEDs) were modulated by using dedicated, high-bandwidth (20 MHz) digital input/output lines (PCI-6534; National Instruments, Austin, TX) followed by MOSFET switches. Fiber bundles measuring 2.5 mm in diameter and 3 m in length (CeramOptec, East Longmeadow, MA) relay light from the LEDs to the subject's head. An average of 0.2 mW at each wavelength for each source position illuminates the subject. Each detector channel has a dedicated avalanche photodiode (C5460-01; Hamamatsu, Tokyo, Japan) digitized by a dedicated 24-bit ADC chip (HD192; MOTU, Cambridge, MA). All data are spooled directly to a hard disk at a sampling rate of 96 kHz, and signal-decoding takes place in software (for further details, see *SI Text*).

Protocol. The research was approved by the Human Research Protection Office of the Washington University School of Medicine, and informed consent was obtained from all participants before scanning. Healthy adult subjects were recruited (two males and five females, ages 23–25). Of the recruited population, one subject (male) was excluded due to poor fit of the imaging cap, and one subject (female) was excluded due to high measurement noise.

Subjects were seated in an adjustable chair facing a 19-inch liquid crystal display at a 70-cm viewing distance. The DOT imaging cap was positioned with the optode array on the back of the head. The nasion-to-top optode row distance was measured to establish repeatable positioning. The cap was centered horizontally with the center of the imaging array near the inion (range across subjects, 0.3 cm below to 2.2 cm above). All presented visual stimuli were radial, reversing, black-and-white grids (10-Hz reversal) on a 50% gray background. The first paradigm consisted of blocks of a 10-sec stimulus followed by a 30-sec 50% gray screen. Stimuli were presented in the order A–B–C (Fig. 3*a*), repeated three times with a gray screen presented 15 sec before and after the stimulus sequence. Each subject returned for three sessions. The second paradigm was an angularly swept radial grid rotated 10 times at 10°/sec (Fig. 5) to complete a sweep of the entire visual field every 36 seconds. Gray screens were also presented for the 45 sec before and 15 sec after the complete sweep sequence.

Analysis. An initial 0.02-Hz, high-pass filter removes long-term drift and all SD pair data were converted to a log-ratio data. Background signals were reduced by following approaches previously demonstrated with fMRI data (60) and simulated near-infrared optical data (61). A global signal derived from nearest-neighbor measurements was removed from SD pair data by linear regression. Starting with the log-ratio optode pair measurments (y_i'), the mean of the first-nearest-neighbor measurements (y_{nn}') is removed from the all y_i' through linear regression by using

$$y_i = y_i' - \frac{\langle y_{nn}, y_i' \rangle}{\langle y_{nn}, y_{nn} \rangle} y_i'.$$

The resulting time traces y_i are then used for reconstruction. Finally, a low-pass filter (0.5 Hz) removed residual pulse signals from the data.

For reconstruction, a two-layer, hemispheric head model (radius = 80 mm) was used with finite-element, forward-light modeling [NIRFAST (62)] to obtain a sensitivity matrix for the optode array. The inverted sensitivity matrix was used to convert time-series measurement data into time-series images of the differential absorption within the head model. Hb_R and HbO_2 concentrations were obtained from the absorption coefficients by using spectral decomposition and the extinction coefficients of Hb_R and HbO_2 at the two wavelengths (for further details, see *SI Text*).

In the eccentricity study (Figs. 3 and 4 and SI Figs. 6 and 7), the images for each subject were coregistered by applying a linear shift transformation to account for intersession variability in cap placement. For each session, the line connecting the centroids of the central lower-right (A) and central lower-left (C) activations was bisected to find the median point. The centroid of each activation was coregistered with a two-dimensional linear transformation. Information about the relative shifts between the activations remained. In the coronal projection view, the three activations have six major positional variables (x and y positions of the center of mass

for each of three activations). After coregistration, four independent variables remained for comparative mapping evaluations. The average shift was 1 cm, with a SD of 6 mm. Due to higher noise, the coregistration was not performed for subject 2.

We thank Gavin Perry for help on the DOT instrumentation and Timothy E. Holy, Linda Larson-Prior, and Samuel Achilefu for helpful comments on the manuscript. This work was supported in part by National Institutes of Health Grants K25NS4339 and R21EB7924.

1. Anderson AW, Marois R, Colson ER, Peterson BS, Duncan CC, Ehrenkranz RA, Schneider KC, Gore JC, Ment LR (2001) *Magn Reson Imag* 19:1–5.
2. Born P, Rostrup E, Larsson HBW, Leth H, Miranda M, Peitersen B, Lou HC (1997) *Perception* 26:758–759.
3. Meek JH, Firbank M, Elwell CE, Atkinson J, Braddick O, Wyatt JS (1998) *Pediatr Res* 43:840–843.
4. Fujiwara N, Sakatani K, Katayama Y, Murata Y, Hoshino T, Fukaya C, Yamamoto T (2004) *NeuroImage* 21:1464–1471.
5. D'Esposito M, Deouell LY, Gazzaley A (2003) *Nat Rev Neurosci* 4:863–872.
6. Obrig H, Villringer A (2003) *J Cereb Blood Flow Metab* 23:1–18.
7. Villringer A, Planck J, Hock C, Schleinkofer L, Dirnagl U (1993) *Neurosci Lett* 154:101–104.
8. Obata T, Liu TT, Miller KL, Luh WM, Wong EC, Frank LR, Buxton RB (2004) *NeuroImage* 21:144–153.
9. Culver JP, Durduran T, Furuya D, Cheung C, Greenberg JH, Yodh AG (2003) *J Cereb Blood Flow Metab* 23:911–923.
10. Wolf M, Wolf U, Toronov V, Michalos A, Paunescu LA, Choi JH, Gratton E (2002) *NeuroImage* 16:704–712.
11. Jasdzewski G, Strangman G, Wagner J, Kwong KK, Poldrack RA, Boas DA (2003) *NeuroImage* 20:479–488.
12. Boden S, Obrig H, Kohncke C, Benav H, Koch P, Steinbrink J (2007) *NeuroImage* 10:1016.
13. Franceschini MA, Fantini S, Thompson JJ, Culver JP, Boas DA (2003) *Psychophysiology* 40:548–560.
14. Culver JP, Siegel AM, Franceschini MA, Mandeville JB, Boas DA (2005) *NeuroImage* 27:947–959.
15. Toronov VY, Zhang XF, Webb AG (2007) *NeuroImage* 34:1136–1148.
16. Gratton G, Corballis PM, Cho E, Fabiani M, Hood DC (1995) *Psychophysiology* 32:505–509.
17. Taga G, Asakawa K, Maki A, Konishi Y, Koizumi H (2003) *Proc Natl Acad Sci USA* 100:10722–10727.
18. Colier W, Quaresima V, Wenzel R, van der Sluijs MC, Oeseburg B, Ferrari M, Villringer A (2001) *Vision Res* 41:97–102.
19. Zaramella P, Freato F, Amigoni A, Salvadori S, Marangoni P, Suppjei A, Schiavo B, Chiandetti L (2001) *Pediatr Res* 49:213–219.
20. Sakatani K, Chen S, Lichty W, Zuo H, Wang YP (1999) *Early Hum Dev* 55:229–236.
21. Kennan RP, Kim D, Maki A, Koizumi H, Constable RT (2002) *Hum Brain Mapp* 16:183–189.
22. Aslin RN, Mehler J (2005) *J Biomed Opt* 10:011009.
23. Wilcox T, Bortfeld H, Woods R, Wruck E, Boas DA (2005) *J Biomed Opt* 10:011010.
24. Gibson AP, Austin T, Everdell NL, Schweiger M, Arridge SR, Meek JH, Wyatt JS, Delpy DT, Hebden JC (2006) *NeuroImage* 30:521–528.
25. Watanabe E, Maki A, Kawaguchi F, Yamashita Y, Koizumi H, Mayanagi Y (2000) *J Biomed Opt* 5:287–290.
26. Buchheim K, Obrig H, von Pannwitz W, Muller A, Heekeren H, Villringer A, Meierkord H (2004) *Neurosci Lett* 354:119–122.
27. Benaron DA, Hintz SR, Villringer A, Boas D, Kleinschmidt A, Frahm J, Hirth C, Obrig H, van Houten JC, Kermit EL, *et al*. (2000) *J Cereb Blood Flow Metab* 20:469–477.
28. Steinbrink J, Wabnitz H, Obrig H, Villringer A, Rinneberg H (2001) *Phys Med Biol* 46:879–896.
29. Kohl-Bareis M, Obrig H, Steinbrink K, Malak K, Uludag K, Villringer A (2002) *J Biomed Opt* 7:464–470.
30. Hebden JC, Gibson A, Yusof RM, Everdell N, Hillman EM, Delpy DT, Arridge SR, Austin T, Meek JH, Wyatt JS (2002) *Phys Med Biol* 47:4155–4166.
31. Selb J, Franceschini MA, Sorensen AG, Boas DA (2005) *J Biomed Opt* 10:011013.
32. Toronov V, Franceschini MA, Filiaci M, Fantini S, Wolf M, Michalos A, Gratton E (2000) *Med Phys* 27:801–815.
33. Boas DA, Chen K, Grebert D, Franceschini MA (2004) *Opt Lett* 29:1506–1508.
34. Joseph DK, Huppert TJ, Franceschini MA, Boas DA (2006) *Appl Opt* 45:8142–8151.
35. Hintz SR, Cheong WF, Van Houten JP, Stevenson DK, Benaron DA (1999) *Ped Res* 45:54–59.
36. Bluestone AY, Abdoulaev G, Schmitz CH, Barbour RL, Hielscher AH (2001) *Opt Expr* 9:272–286.
37. Rosa MGP, Soares JGM, Fiorani M, Gattass R (1993) *Vis Neurosci* 10:827–855.
38. Felleman DJ, Van Essen DC (1991) *Cereb Cortex* 1:1–47.
39. Gilbert CD, Wiesel TN (1979) *Nature* 280:120–125.
40. Talbot SA, Marshall WH (1941) *Am J Ophthalmol* 24:1255–1263.
41. Spalding JMD (1952) *J Neurol Neurosurg Psychiatry* 15:169–183.
42. Harding GFA, Janday B, Armstrong RA (1991) *Brain Topography* 4:47–55.
43. Fox PT, Mintun MA, Raichle ME, Miezin FM, Allman JM, Van Essen DC (1986) *Nature* 323:806–809.
44. Fox PT, Perlmutter JS, Raichle ME (1985) *J Comput Assist Tomogr* 9:141–153.
45. Belliveau JW, Kennedy DN, Mckinstry RC, Buchbinder BR, Weisskoff RM, Cohen MS, Vevea JM, Brady TJ, Rosen BR (1991) *Science* 254:716–719.
46. Engel SA, Glover GH, Wandell BA (1997) *Cereb Cortex* 7:181–192.
47. Kang HC, Burgund ED, Lugar HM, Petersen SE, Schlaggar BL (2003) *NeuroImage* 19:16–28.
48. Colak SB, van der Mark MB, Hooft GW, Hoogenraad JH, van der Linden ES, Kuijpers FA (1999) *IEEE J Quantum Electron* 5:1143–1158.
49. Schmitz CH, Graber HL, Luo HB, Arif I, Hira J, Pei YL, Bluestone A, Zhong S, Andronica R, Soller I, *et al*. (2000) *Appl Opt* 39:6466–6486.
50. McBride TO, Pogue BW, Jiang S, Osterberg UL, Paulsen KD (2001) *Rev Sci Instrum* 72:1817–1824.
51. Culver JP, Siegel AM, Stott JJ, Boas DA (2003) *Opt Lett* 28:2061–2063.
52. Stensaas SS, Eddington DK, Dobelle WH (1974) *J Neurosurg* 40:747–755.
53. Fox PT, Miezin FM, Allman JM, Van Essen DC, Raichle ME (1987) *J Neurosci* 7:913–922.
54. Wandell BA, Brewer AA, Dougherty RF (2005) *Philos Trans R Soc London Ser B* 360:693–707.
55. Sereno MI, Dale AM, Reppas JB, Kwong KK, Belliveau JW, Brady TJ, Rosen BR, Tootell RBH (1995) *Science* 268:889–893.
56. Huppert TJ, Hoge RD, Diamond SG, Franceschini MA, Boas DA (2006) *NeuroImage* 29:368–382.
57. Cannestra AF, Bookheimer SY, Pouratian N, O'Farrell A, Sicotte N, Martin NA, Becker D, Rubino G, Toga AW (2000) *NeuroImage* 12:41–54.
58. Boas DA, Culver JP, Stott JJ, Dunn A (2002) *Opt Expr* 10:159–170.
59. Gibson AP, Riley J, Schweiger M, Hebden JC, Arridge SR, Delpy DT (2003) *Phys Med Biol* 48:481–495.
60. Fox MD, Snyder AZ, Vincent JL, Corbetta M, Van Essen DC, Raichle ME (2005) *Proc Natl Acad Sci USA* 102:9673–9678.
61. Saager RB, Berger AJ (2005) *J Opt Soc Am A* 22:1874–1882.
62. Dehghani H, Pogue BW, Poplack SP, Paulsen KD (2003) *Appl Opt* 42:135–145.